RSC Advances

PAPER

View Article Online
View Journal | View Issue

Cite this: *RSC Adv.*, 2024, **14**, 3867

Ag_2O@UiO-66 new thin film as p–n heterojunction: permanent photoreduction of hexavalent Cr

Sara Amiri,[a] Mohammad Chahkandi *[a] and Mahboobeh Zargazi[b]

Received 15th September 2023
Accepted 16th January 2024

DOI: 10.1039/d3ra06305d

rsc.li/rsc-advances

The new nanosphere Ag_2O@UiO-66 thin-film was synthesized on a stainless steel mesh surface *via* an electrophoretic deposition method, and is used as an effective and low-cost photocatalyst using visible light. The synthesized nanocomposite was used to perform photo-reduction of Cr(VI) ions under white light irradiation. The best removal rate (72% after 15 minutes) was obtained by the film with 0.034 grams of deposited composite having relative percentages of Ag_2O : UiO-66 of 70 : 30. The interesting obtained results confirm that the p–n heterojunction of the composite is the main cause of the desired charge separation and the photoreduction speed increase. In the following, the resulting compounds were characterized by X-ray diffraction (XRD), Fourier transform infrared (FT-IR), transmittance electron microscopy (TEM), field emission scanning electron microscopy (FE-SEM), energy diffraction X-ray spectroscopy (EDAX) and the Brunauer, Emmett, and Teller (BET) method. Scavenging studies performed in the presence of familiar scavengers confirmed that superoxide radicals ($^{\bullet}O_2^-$) and dissolved oxygen gas have a significant role in the photocatalytic reduction process.

1 Introduction

Toxic and harmful pollutants such as chemical azo dyes, phenols, Cr(VI), pesticides, and industrial effluents, often receive minimal treatment before entering the environment. These pollutants are not only dangerous for humans, but also threaten marine and soil life.[1,2] Cr(VI) has a destructive effect on humans and fauna after entering groundwater from sewage from metallurgy, dyeing, electroplating, and leather tanning industries,[3–5] as well as volcanic activities, forest fires, and weathering of pyroxene from natural sources.[6]

The oxidation states of chromium are responsible for its detrimental environmental effects.[7] Chromium(VI) is soluble and easily migrates in water, and it is 500–1000 times more poisonous than chromium(III), having carcinogenic and mutagenic effects on living organisms.[8] Therefore, one applicable remediation method for chromium(VI) is reduction of this very toxic form to chromium(III) with less toxicity and greater perceptibility.

So far, different approaches have been applied to the reduction and toxic depletion of chromium(VI), including chemical precipitation, photocatalytic remediation, bacterial regeneration, absorbing on activated carbon, membrane process and bioremediation.[9–15]

However, some of these methods have disadvantages such as being expensive, short usage period, needing advanced techniques and tools, as well as the probability of secondary pollution.[8,16] Photocatalytic reduction of chromium(VI) as a reliable and inexpensive method and is known as a cleaner and more practical approach than chemical reduction. This process includes some advantages like capability of fuelling with clean solar energy, having high catalytic performance, no sludge formation, no secondary pollution by non-reduced Cr(VI), and no need for a large amount of chemical reagents.[17,18] Considering the unlimited supply of solar energy, photocatalysis technology is a very effective procedure for purifying heavy metal ions as well as organic pollutants in order to reduce environmental contamination.[19]

However, many photocatalysts introduced for the photoreduction of chromium(VI), contain metal oxides, perovskites, C-based compounds, metal organic frameworks (MOFs) and so forth. Cr(VI) can be quickly and easily reduced with a mixture of TiO_2 and titanate nanotubes (TNT) as the photocatalyst, in a one-step method.[20] Graphitic carbon nitride as a less toxic metal-free photocatalyst has been used for the reduction of Cr(VI) under visible light.[21] Bi_2S_3 with a direct band gap of 1.3 eV has shown good photocatalytic activity for the reduction of Cr(VI) exposed to visible light.[22,23] The composite synthesis of two photocatalysts (due to their synergistic effect in better electron–hole separation), doping of semiconductors with metal cations (improving the absorption of light and separation of photogenerated charge carriers) and p–n heterojunction structure (to effectively suppress electron–hole recombination) can increase the photocatalytic performance.[17] Cu_2O/Bi_5O_7I,[24]

[a]*Department of Chemistry, Hakim Sabzevari University, Sabzevar, 96179-76487, Iran. E-mail: m.chahkandi@hsu.ac.ir; Fax: +985144013501; Tel: +985144013525*

[b]*Sonochemical Research Center, Department of Chemistry, Faculty of Science, Ferdowsi University of Mashhad, Mashhad, Iran*

$Fe_3O_4/FeWO_4$,[25] Zr-SnS_2/PANI,[26] and rGO@$Cu_2O/BiVO_4$,[27] are such examples in the photocatalytic reduction of Cr(VI). It has been found that the photocatalytic reduction capability of semiconductors is more dependent on the available active sites for Cr(VI) reduction than their surface area.[28]

MOFs are crystalline structures with a strong network formed by interactions between organic linkers and metal clusters, they possess various attractive features such as an inherent and permanent porous structure with adjustable pore size, ultra-high surface area, polymetallic sites, and thermal stability.[29–31] UiO-66 is a zirconium-based MOF with high structural stability in aqueous media that can be used as a photocatalyst for the removal of heavy metals, including Cr(VI).[32,33] Among the p-type semiconductors, Ag_2O seems to be very desirable in terms of low band gap (~1.4 eV), good matching, and low price capable of creating valuable p–n junctions with n-type semiconductors. Nowadays, p–n junctions are considered an alternative method to enhance photo-generated charge separation to create an efficient internal electric field (IEF) at the interface of p-type and n-type semiconductors.

Ag_2O/Bi_2WO_6, Ag_2O/TiO_2, and Ag_2O/Fe_2O_3 having p–n junction character, are known as efficient heterostructures for photocatalysis. Previous studies have reported the p–n junction of Ag_2O and UiO-66.[34,35]

Following our previous studies on the design and synthesis of new photocatalysts,[10,36–39] in this work, for the first time, a Ag_2O@UiO-66 thin-film was deposited on a steel mesh by electrophoretic deposition. This resulted in a metal–organic framework thin-film composite which we used as an efficient visible light active photocatalyst for the reduction of toxic chromium(VI) to non-toxic chromium(III) in aqueous solution.

2 Experimental

2.1 Materials

All chemicals are analytical reagent grade purchased from Fluka and Merck companies and employed as received without additional purification. They are zirconium(IV) chloride ($ZrCl_4$), silver nitrate ($AgNO_3$), isopropanol (IPA), sodium iodate ($NaIO_3$), sodium azide (NaN_3), dimethylformamide (DMF), hydrochloric acid (HCl), terephthalic acid ($C_6H_4(CO_2H)_2$), ethanol (EOH), and deionized (DI) water.

2.2 Preparation of UiO-66

A mixture of zirconium chloride (0.54 mmol, 0.09 M), 5 mL dimethylformamide (DMF) solvent, and 1 mL hydrochloric acid (33%) was sonicated for 20 minutes until fully dissolved. 123 mg terephthalic acid (0.75 mmol, 0.075 M) dissolved in 10 mL DMF was added to the above solution and was sonicated, again for 20 minutes. Next, the resulting mixture was transferred to the autoclave and heated in the oven at 80 °C for 24 h. The obtained white solid was collected and washed twice with DMF and ethanol and heated under vacuum at 90 °C for an additional 24 hours, until the solvents were completely dried and the final activated sample was prepared.[40]

2.3 Preparation of Ag_2O

Ag_2O nanoparticles (NPs) were prepared *via* the modified method proposed by Kadam *et al.*[41] According to this procedure, 0.7 g NaOH (0.12 M) was dissolved in 150 mL DI water and then it was added dropwise to a solution of 0.3 g $AgNO_3$ (0.012 M) dissolved in 150 mL DI water under ambient conditions. The obtained precipitate was collected by centrifugation and washed several times with distilled water. Finally, the powder was dried overnight at room temperature (R.T., 25 °C).

2.4 Functionalization of Ag_2O NPs with UiO-66: thin film coating

The new Ag_2O@UiO-66 composite was synthesized *via* an impregnation method.[42] First, the MOF powder (50 mg, 0.21 M) was immersed in a mixture of 30 mg silver nitrate ($AgNO_3$, 0.64 M) and dissolved in 8 mL acetonitrile. The obtained solution was stirred at R.T. for 4 h to form an impregnated brownish suspension. After that, the mixture was centrifuged to separate the solid part and then washed three times with acetonitrile. The composite Ag_2O@UiO-66 was annealed in an oven for 2 h at 130 °C. A stable suspension of the composite NPs (0.01–0.07 g) were ultrasonically (BRANSON bath, 40 kHz) dispersed in 20 mL acetone. Finally, the intended thin films of Ag_2O@UiO-66 were coated on polished commercial steel mesh substrates (2 cm^2) using the prepared suspension, through an electrophoretic deposition (EPD) process. A similar substrate chosen as the cathodic electrode was located at a center to center distance of 6.5–23 mm from the anodic electrode. EPD was carried out under potentiostatic conditions using a DC power supply (TF 102, TERCO) and applied voltages of 60 to 110 volts. A variety of deposited layers having different thicknesses and coating weights were prepared *via* manipulation of the initial concentration of suspension, applied voltage, and the distance between the electrodes. The prepared films were dried at R.T. The yield of electrophoretic deposition for each film was measured from the weighted difference between the initial bare electrode and the final coated electrode.

2.5 Characterization of Ag_2O@UiO-66 film

Crystal structure, phase identity, and purity of the samples were characterized using powder X-ray diffraction (PXRD, DMAX-2500, Rigaku) with 1.54 Å wavelengths of Cu Kα radiation at a scanning rate of 3° min^{-1} from 5° to 80° (2θ). Fourier transform infrared (FT-IR; Shimadzu 8700) was used for vibrational analysis and structural determination, recorded at R.T. with KBr pellets in the range 500–4000 cm^{-1}. Transmittance electron microscopy (TEM; eFM208Se-USA) analysis was employed for particle size and morphology survey of the synthesized compounds. Shape and elemental analysis were determined using field emission scanning electron microscopy (FE-SEM; Mira TESCAN) equipped with elemental mapping (EM) and energy diffraction X-ray spectroscopy (EDAX). The specific surface area of samples was measured using the Brunauer, Emmett, and Teller (BET) method (AUTOSORB-1, Quantachrome Instruments Inc., USA). Photocatalytic studies were

accomplished under light irradiation (LED lamp, 200 W). A Photonix UV-visible array spectrophotometer (EU-2200) was utilized to investigate the visible light photocatalytic activity of the samples.

2.6 Photocatalytic activity of Ag_2O@UiO-66 film

Thin films of the various composites with different relative percentages of Ag_2O and UiO-66 (Ag_2O/UiO-66%: 20/80, 30/70, 40/60, 50/50, 60/40, 70/30, and 80/20) were produced using the EPD method, and their catalytic efficiency for Cr(VI) reduction were assessed and compared. The photocatalytic capability of the Ag_2O@UiO-66 thin film and its components, for the reduction of aquatic hexavalent chromium (Cr(VI)) was studied. Contaminated model solutions were prepared by dissolving potassium dichromate ($K_2Cr_2O_7$) (20 ppm) in DI water. The Ag_2O@UiO-66 film was hung in 50 mL of 20 ppm chromium(VI) solution and the aqueous concentration of Cr(VI) was measured using a UV-visible optical spectrometer. First, the samples were magnetically stirred for 60 min in the dark at R.T. (based on the Max. wavelength assessment using UV spectra) to achieve absorption/desorption equilibrium, they were then irradiated for 120 minutes under a 200 W visible light LED lamp. The amount of reduced Cr(VI) can be obtained from eqn (1):

$$A = \log I/I_0 \quad (1)$$

where I indicates the present concentration of Cr(VI) and I_0 the initial one. The ion shows an absorption maximum wavelength at 350 nm. After turning on the LED light, 3 mL of the 20 ppm chromium(VI) solution was removed every 5 minutes and centrifuged at 3500 rpm for 3 minutes. The clear supernatant solution was transferred into quartz cells with a syringe and using UV-vis analyses, the amount of chromium(VI) present in solution and the reduced ion were collected. To further study the photocatalytic degradation, the desorption of pollutant ions from the catalytic surface was evaluated in 0.005 M acidic solution both in the dark and under light illumination.

In order to specify the reactive species during the photocatalytic process, the proper radical scavengers were examined. They are ethanol (EOH), isopropanol (IPA), sodium iodate ($NaIO_3$), and sodium azide (NaN_3) as scavengers for hydroxyl free radicals ($^{\bullet}OH$), holes (h^+), electrons (e^-), and superoxide radicals ($^{\bullet}O_2^-$), respectively. To investigate the effect of dissolved oxygen, nitrogen gas was purged in the suspension during the photocatalytic process. Mott–Schottky (M–S) analysis was carried out at a fixed frequency of 1000 Hz for the synthesized composite and its components after immersion in 0.5 M Na_2SO_4 solution for 24 h. Electrochemical impedance spectroscopy (EIS) was employed to investigate the interface of the photocatalyst and solution under light irradiation.

3 Results and discussion

3.1 Structural recognition of Ag_2O@UiO-66

The physicochemical and morphological features of the synthesized Ag_2O@UiO-66 nano-photocatalyst, Ag_2O, and UiO-66 components were studied using various techniques including FT-IR, XRD, SEM, TEM, EM, and BET.

FTIR is a popular method based on the vibrations of atoms within a molecule which is used to obtain data about functional groups. Fig. 1a shows the FTIR spectra of the prepared Ag_2O, UiO-66, and synthesized Ag_2O@UiO-66 in the range 500 and 4000 cm^{-1}. The presence of benzene rings and carboxylate moiety in UiO-66 can be confirmed based on the recorded vibrations. The broad strong peak between 3000 and 3600 cm^{-1} corresponds to the vibration of O–H groups, and the weak transmittance peak at 1700 cm^{-1} could be due to the stretching modes of C=O from free carboxylic groups on the surface of MOFs.[43] The moderate band observed at 1590 cm^{-1} is related to the C=O stretching, while the benzene ring C=C bond is detected by the strong stretching peak at 1420 cm^{-1}.[3] The moderate peak at 745 cm^{-1} illustrates the twisting and bending of the Zr nodes.[44] The moderate bands at 670 cm^{-1} and 510 cm^{-1} are attributed to Zr–O and Zr–O–Zr stretching, respectively.[45] In the FT-IR spectra of Ag_2O@UiO-66 and Ag_2O,

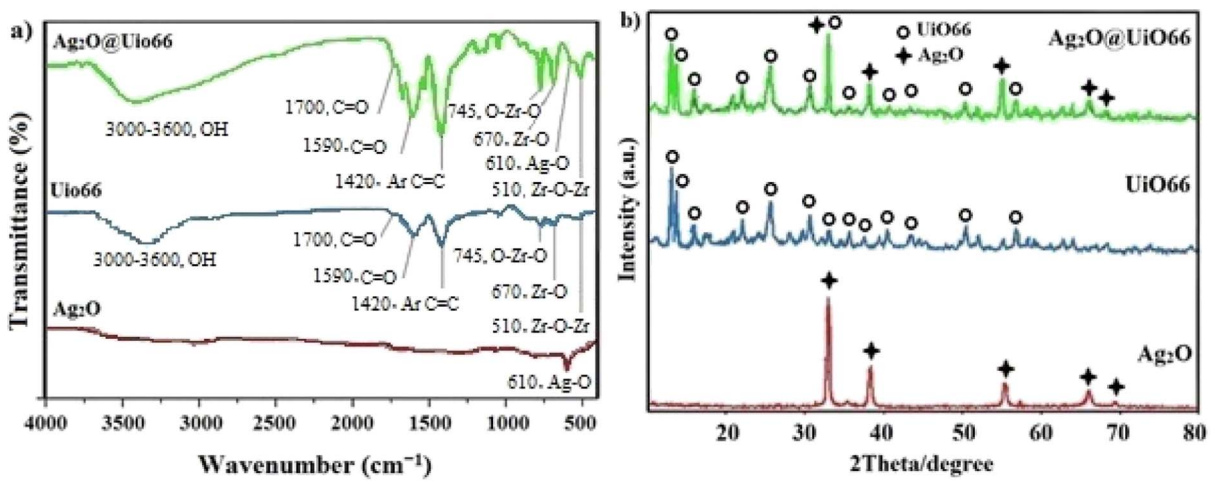

Fig. 1 (a) The FT-IR spectrum and (b) wide-angle XRD patterns.

the weak band appearing at 610 cm^{-1} can be attributed to the vibration of the Ag–O bond.[46] All of the observed peaks of the compounds in Fig. 1a confirm the proposed structures.

X-ray diffraction is a non-destructive technique used for the recognition of crystal structure and NP purity. Each crystalline solid has a different atomic structure and therefore a unique X-ray diffraction pattern, which can be used as the fingerprint for the recognition of the crystal structure.[47] Therefore, the crystalline structure pattern showing the successful synthesis, is shown in Fig. 1b. The five characteristic diffraction peaks of the Ag_2O NPs appeared at $2\theta = 32.53°$, 38.11°, 55.01°, 65.65°, and 69.00° corresponding to miller indexes of 111, 200, 220, 311, and 222, respectively, which are matched to the Ag_2O FCC crystalline phase (JCPDS 041-1104).[48] In the XRD pattern of the prepared UiO-66, the peaks recorded at $2\theta = 7.2$, 8.45, 14.8, 17.53, 22.35, 25.7, 30.8, 33.25, 36.2, 37.45, 40.7, 43.5, 50.3, and 57.1° are associated with 111, 200, 222, 400, 511, 600, 711, 553, 731, 820, 751, 664, 933, and 1242 crystalline planes.[49] Also, the pattern of Ag_2O@UiO-66 was well fitted with the data of Ag_2O and UiO-66. These results confirm that Ag_2O@UiO-66 was properly synthesized.

The average crystallite size of Ag_2O, UiO, and Ag_2O@UiO-66 samples were estimated as 14, 70, and 110 nm, respectively, using the Debye–Scherrer equation (eqn (2)):[46]

$$D = K\lambda/\beta_{1/2}\cos\theta \quad (2)$$

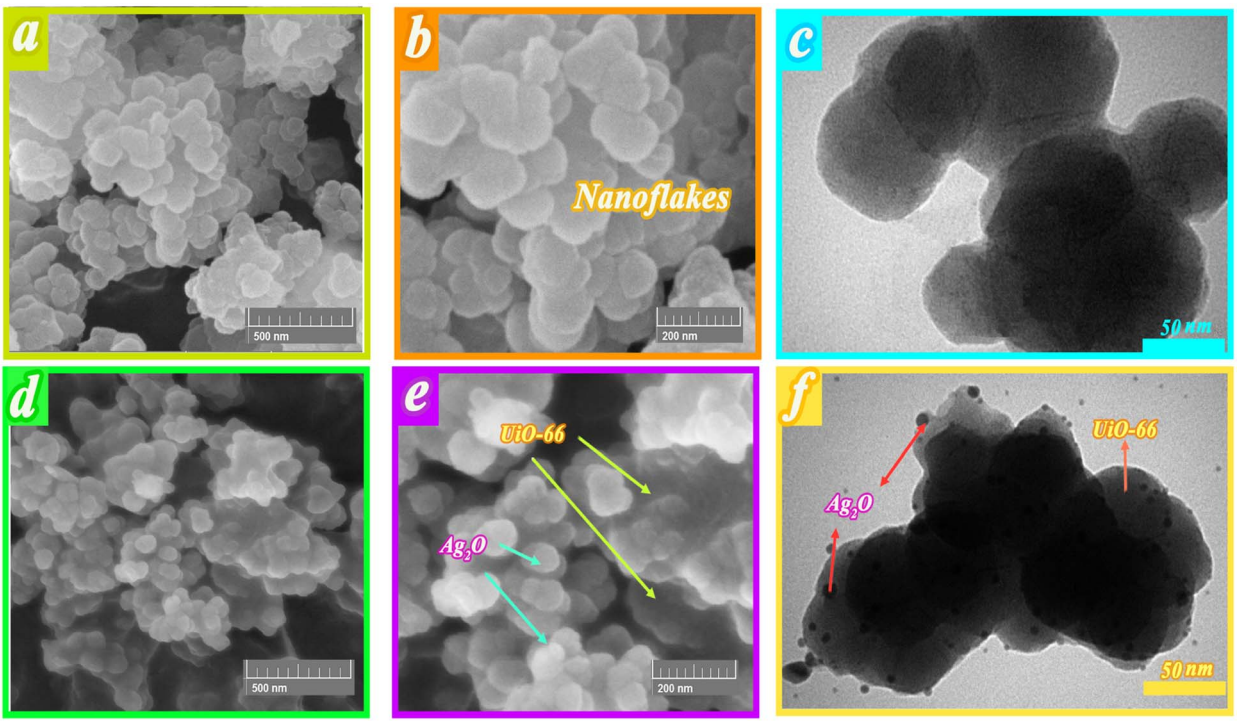

Fig. 2 (a and b) FE-SEM images of UiO-66, (d and e) FE-SEM images of Ag_2O@UiO-66, (c) TEM of UiO-66, and (f) TEM of Ag_2O@UiO-66.

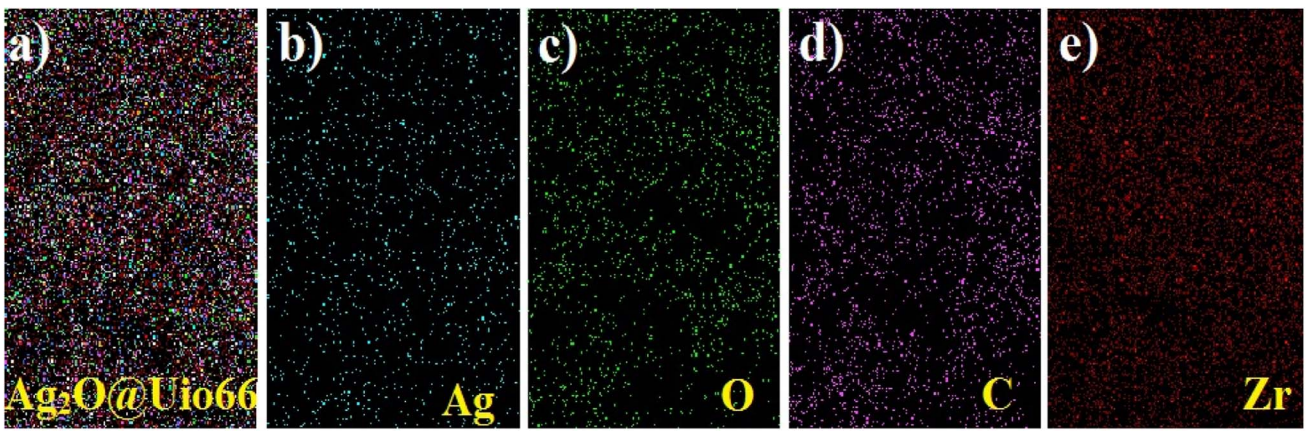

Fig. 3 Elemental mapping of Ag_2O@UiO-66, and the Ag, O, C, and Zr elements.

where K is the dimensionless shape constant, λ is the wavelength of the X-ray, and $\beta_{1/2}$ is the full width at peak's half maximum.

SEM images were utilized to investigate the particle size and surface morphology of the prepared UiO-66 (Fig. 2a and b) and the synthesized Ag_2O@UiO-66 NPs (Fig. 2d and e). As can be seen from Fig. 2a and b, UiO-66 films have a flake-like morphology with size in the range 89–107 nm. The increasing composite size compared to the UiO-66 component, is due to combination with Ag_2O (Fig. 2d and e). The SEM images obviously display the synthesized Ag_2O NPs with a narrow and uniform size distribution without obvious agglomeration. Clearly, the observed size from the SEM images are in good agreement with those calculated from the Debye–Scherrer equation.

The TEM image of the UiO-66 nanocomposite confirm the flake-like morphology of nanocrystals with a diameter size around 88 nm (Fig. 2c). Likewise, Ag_2O NPs have a diameter size in the range 8 nm, well dispersed over the surface of UiO-66 with uniform size (Fig. 2f).

EM analysis of Ag_2O@UiO-66 in different selected areas is shown in Fig. 3, which evidently shows the monotype dispersion of Ag, O, C, and Zr. It can be concluded that the SEM and EM results confirm the successful synthesis of the Ag_2O@UiO-66 nanocomposite because of the presence of all the main included elements with accurate intensities shown by the appropriate colors (ref. to Fig. 3b–e). As can be seen, Zr has a higher density than Ag, as it is the main building block of the material.

The elemental percentages for UiO-66 and Ag_2O@UiO-66 compounds are depicted in Fig. 4 and clearly include the main peaks of Zr, O, C, and, Ag. Therefore, the synthesis of UiO-66 and Ag_2O composites is again proven.

The surface area and pore distribution of Ag_2O, UiO-66, and Ag_2O@UiO-66 were analyzed using nitrogen adsorption–desorption isotherms at 77 K (Fig. 5a). The pore size

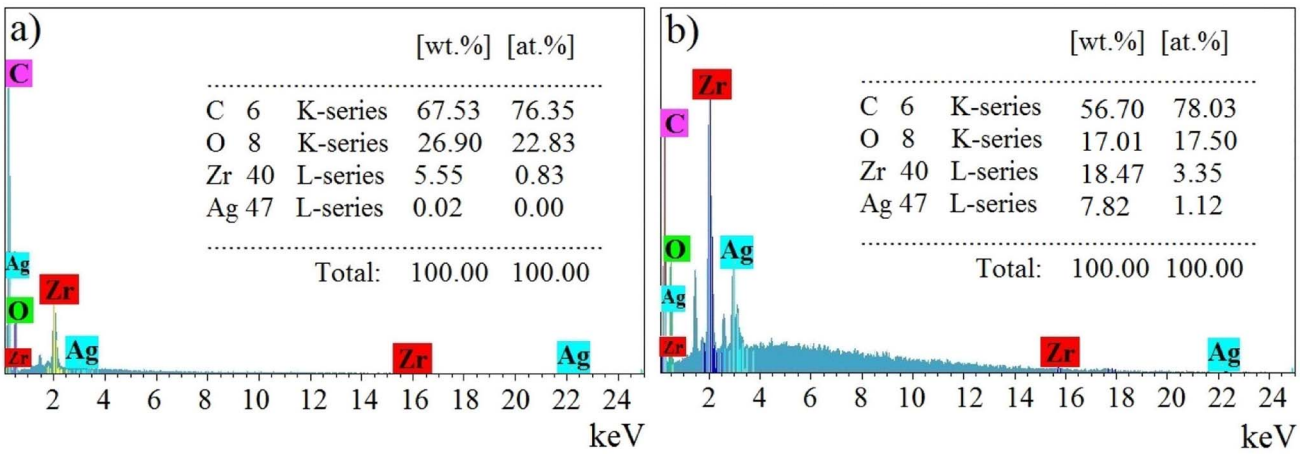

Fig. 4 The EDAX of (a) UiO-66 and (b) Ag_2O@UiO-66 compounds.

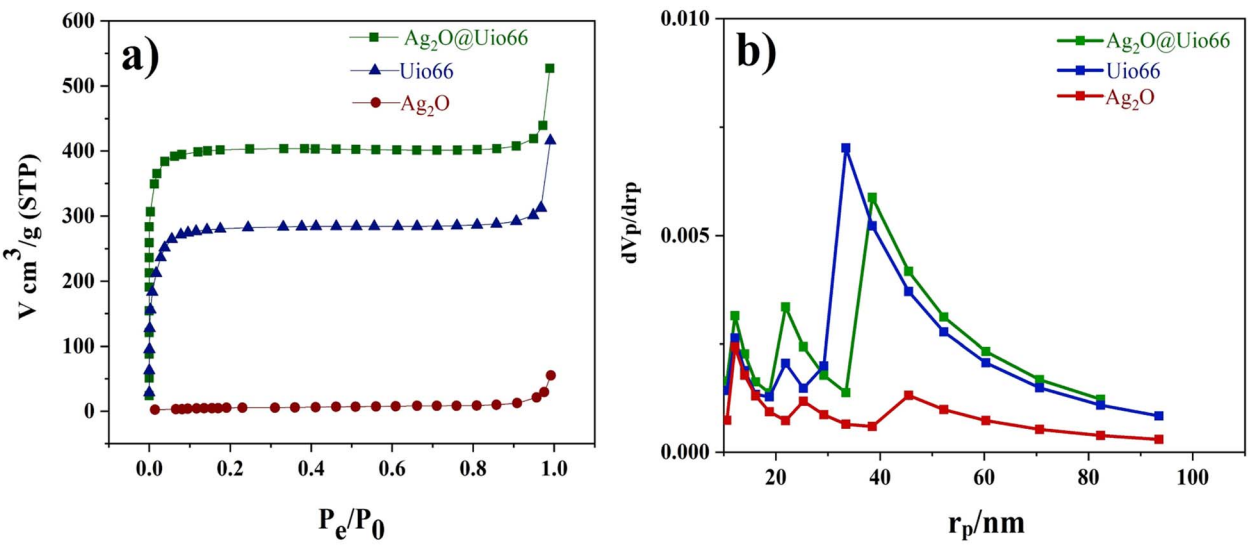

Fig. 5 (a) N_2 adsorption–desorption isotherms and (b) pore size distribution based on the BJH for Ag_2O, UiO-66, and Ag_2O@UiO-66.

Table 1 Texture properties of pure Ag_2O, UiO-66, and Ag_2O@UiO-66. SA_{BET} stands for BET surface area, SA_{Lang} stands for Langmuir surface area, V_{total} stands for total pore volume, and r_p stands for average pore diameter

Sample	SA_{BET} ($m^2\ g^{-1}$)	SA_{Lang} ($m^2\ g^{-1}$)	V_{total} ($cm^3\ g^{-1}$)	r_p (nm)
Ag_2O	20.983	32.708	0.080782	15.4
UiO-66	1098.2	1246.2	0.6397	2.3298
Ag_2O@UiO-66	943.97	1757	0.8151	3.4538

distribution of Ag_2O, UiO-66, and Ag_2O@UiO-66 were calculated using the BJH method in the range 1–100 nm (Fig. 5b). The detailed properties of Ag_2O, UiO-66, and Ag_2O@UiO-66 – the BET surface area, Langmuir surface area, total pore volume, and average pore diameter – are summarized in Table 1. Adsorption–desorption Langmuir isotherms of UiO-66 and Ag_2O@UiO-66 conform with type 2. The absorbance values of Ag_2O, UiO-66, and Ag_2O@UiO-66 were determined as 20.983, 1098.2, and 943.97 $m^2\ g^{-1}$, respectively. Something that is obvious is that the specific surface area of Ag_2O@UiO-66 is greater than that of Ag_2O and UiO-66, which results in higher photocatalytic activity of the composite (refer to Section 3.2). There is an impressive rise of volume *versus* low pressure condition for UiO-66 and notably Ag_2O@UiO-66 that indicates the highly porous structure for those mentioned compounds (see Fig. 5a).[50] However, observation of high adsorption capacity at a relatively high pressure ($P/P_0 > 0.8$) suggests the coexistence of mesopores and macropores spread out.[51]

3.2 Photocatalytic effect of Ag_2O@UiO-66

To investigate the photocatalytic properties of Ag_2O@UiO-66 and compare it with its constituent components, 0.03 grams of each of Ag_2O, UiO-66, and Ag_2O@UiO-66 were transferred separately to beakers containing 50 mL of 20 ppm chromium(VI) solution under 200 W LED white light. The photocatalytic effect of the Ag_2O@UiO-66 composite was compared with its components, and the results are shown in Fig. 6a. The respected graphs were drawn based on C_t/C_0 *vs.* time using the removal rate measured by eqn (3),

$$\text{Removal rate} = \frac{C_0 - C_t}{C_0} \times 100 \quad (3)$$

where C_t is the concentration of chromium(VI) at time t and C_0 is the initial concentration of chromium(VI). The components of the composite showed a lower removal rate compared to the composite itself: Ag_2O@UiO-66 was able to photoreduce 72% of chromium(VI) under LED light in 20 minutes.

In the study of the absorption spectrum, the electronic structure of the material can be directly determined by examining the electron moving from the valence band (VB) to the conduction band (CB) using an ultraviolet-visible device. The electronic transfer spectra of Ag_2O, UiO-66, and Ag_2O@UiO-66 are shown in Fig. 6b. In addition, the optical band gap energy (E_g) of samples was obtained by the Tauc equation (eqn (4)),

$$(\alpha h\nu)^{\gamma} = A(h\nu - E_g) \quad (4)$$

where α, h, and, ν are absorption coefficient, Planck's constant, and frequency, respectively. A is the optical transition-dependent constant of the investigated material and γ represents the nature of electron transfer in the semiconductor. The optical band gap energy can be assessed by extrapolating the linear portion near the onset on the plot of *versus* $h\nu$. The band gap energies of 1.59, 3.37, and 2.03 eV were evaluated for Ag_2O, UiO-66, and Ag_2O@UiO-66, respectively.

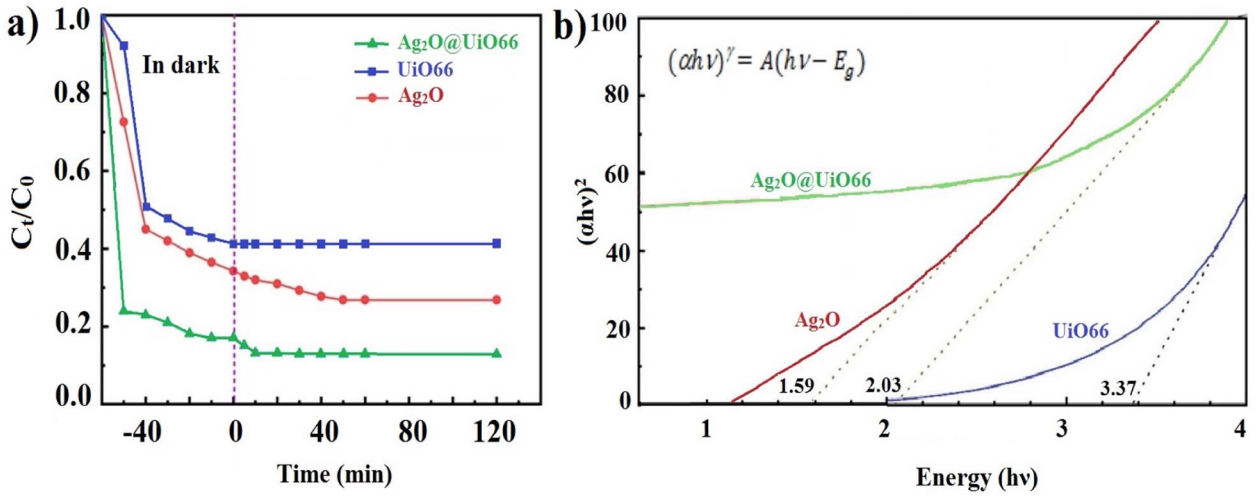

Fig. 6 (a) Comparison of the removal rate of Ag_2O@UiO-66 with Ag_2O and UiO-66, (b) electron transfer spectrum of Ag_2O, UiO-66 and Ag_2O@UiO-66.

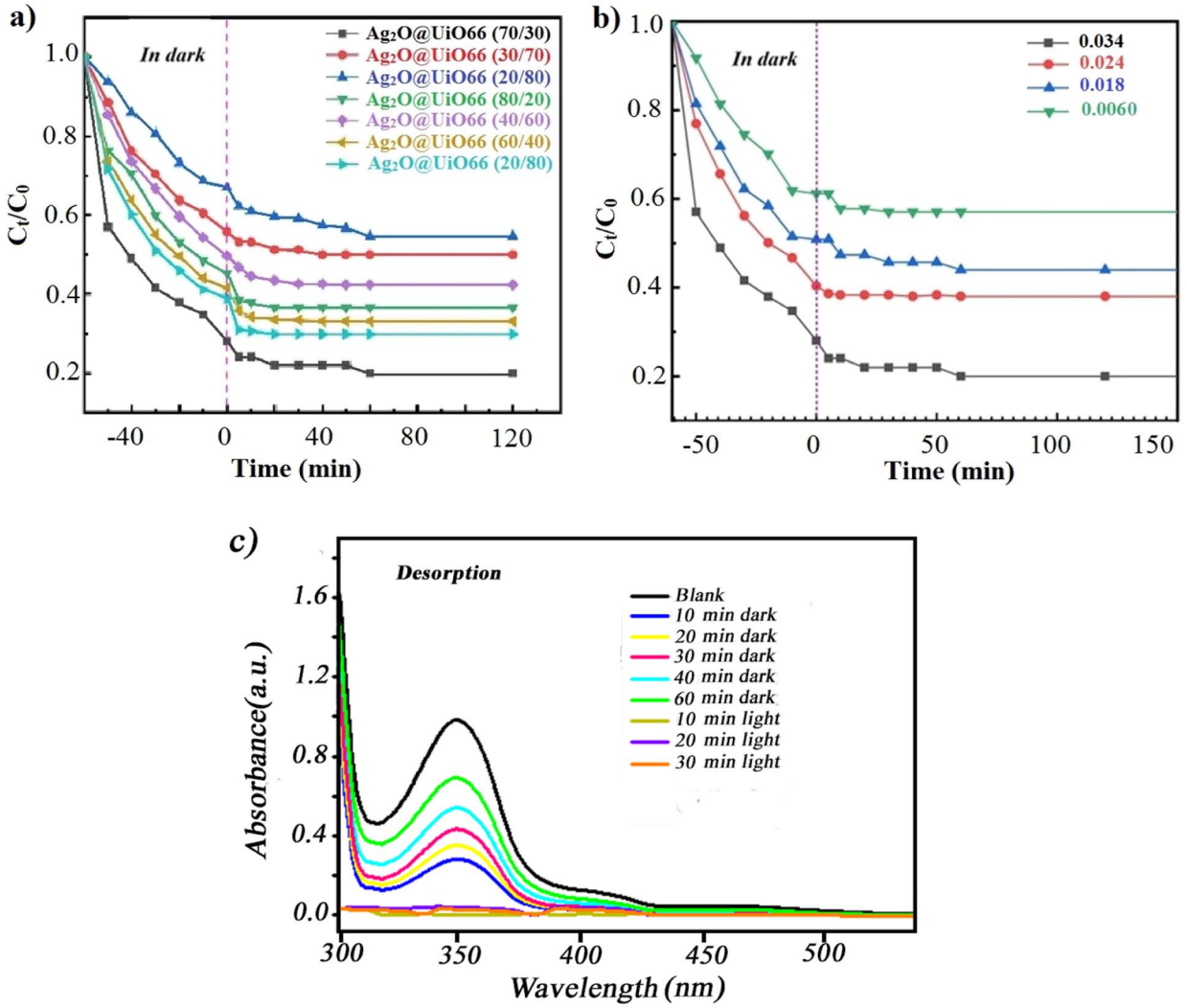

Fig. 7 Cr(VI) removal rate by Ag_2O@UiO-66 films (a) different percentages of components of Ag_2O@UiO-66, (b) various weights of coated films, (c) curves of the desorption process for optimal thin film (Ag_2O@UiO-66 (70/30) with 0.034 g amount of film) in the dark and under light irradiation.

Due to the lower *Eg* of the composite compared to UiO-66, electron transfer from the VB to CB and subsequent creation of holes in the VB of the composite happens more easily than in UiO-66. As a result, the composite shows a higher removal rate than UiO-66.

After ensuring the better removal rate of Ag_2O@UiO-66 compared to its components (Fig. 6a), composites with different relative percentages of Ag_2O and UiO-66 (Ag_2O/UiO-66: 20/80, 30/70, 40/60, 50/50, 60/40, 70/30 and 80/20) were prepared and the removal rate of these new composites were compared with each other. 0.03 g of the obtained composites was transferred to a beaker containing 50 mL of 20 ppm chromium(VI) solution and placed on a magnetic stirrer at room temperature and in the dark. After 60 minutes passed and the absorption–desorption balance was established, the samples were placed under the LED lamp. 3 mL of 20 ppm chromium(VI) solution was picked up at certain times (every 5 minutes) and after centrifuging at 3500 rpm for 3 minutes, the clear supernatant solution was poured into quartz cells and the reduction of chromium(VI) was checked using a UV-vis spectrometer. The best chromium(VI) reduction rate was obtained by the composite 70/30 Ag_2O@UiO-66 (Fig. 7a). Eventually, four different weights of coated film were produced using the EPD process and the related chromium(VI) reduction was examined. The best rate for chromium reduction (72% after 15 minutes) was obtained by the film with 0.034 grams of deposited composite (see Fig. 7b). It seems that the catalytic surface of the Ag_2O@UiO-66 (70/30) film is very active and the adsorbed pollutant Cr(VI) ions are completely reduced on the surface. Fig. 7c depicts the UV-vis spectra of the desorbed solution during the adsorption and degradation process in the dark and under light illumination. As can be obviously observed, under dark conditions the adsorbed pollutant Cr(VI) ions were desorbed from the thin film surface, while the recorded desorption rate under light illumination (10 to 30 minutes) is not significant and can be ignored. These findings confirm that the photocatalytic degradation occurred efficiently on the thin film surface.

3.3 Influence of active species scavengers

To understand how the impressive agents work, some familiar scavengers were used in the current photocatalytic reaction. Ethanol, isopropanol, sodium iodate, and sodium azide were used as scavengers for holes (h^+), hydroxyl free radicals ($^{\bullet}OH$), electrons (e^-) and superoxide radicals ($^{\bullet}O_2^-$), respectively. As shown in Fig. 8a, the removal rate of Cr(VI) was improved when ethanol was present in the solution. This can be attributed to the decrease of the recombination rate of the hole–electron in the presence of ethanol as a hole scavenger.[10] This result is also in consistent with the findings of Du *et al.*[3] and Li *et al.*[33] who showed that hole scavengers can enhance the photo-induced charge carrier separation to increase the Cr(VI) reduction. In the presence of other scavengers, the removal rate of Cr(VI) was decreased, which indicates the effect of the investigated active species in the reaction process. By checking the results of scavenging studies, it is highlighted that superoxide radicals and dissolved oxygen gas play a main role in the photocatalytic reduction process.

3.4 Stability and recycling of Ag_2O@UiO-66 thin film

Fig. 8b, plainly demonstrates the high reusability and stability of the Ag_2O@UiO-66 thin film in the photocatalytic reduction of Cr(VI) over five runs. There is an 11% decrease in removal rate after five cycles which can be attributed to the loss of photocatalyst mass during separation and photocatalyst washing after each run. To ensure the stability of the photocatalyst structure during the recycling process, the XRD and TEM of the sample after five runs was compared with that of the fresh one (Fig. 8c and d). The results show that XRD of the reused photocatalyst after five runs is nearly the same as the fresh one and no meaningful changes can be observed in the basic peak positions. In the TEM image of the recycled photocatalyst, Ag_2O particles are still easily recognizable. Therefore, it can be concluded that, no significant leaching would happen in the reused photocatalyst structure. Based on the inset figure in Fig. 8d, the SEM of the Ag_2O@UiO-66 thin film after Cr(VI) reduction does not show any permanent morphological changes.

3.5 Mott–Schottky and Nyquist curves

The photocatalytic performance of Ag_2O@UiO-66 and UiO-66 were compared by measuring the number of photogenerated electron holes (N_D) on the catalyst surface and flat band potential (V_{fb}) using M–S analysis:

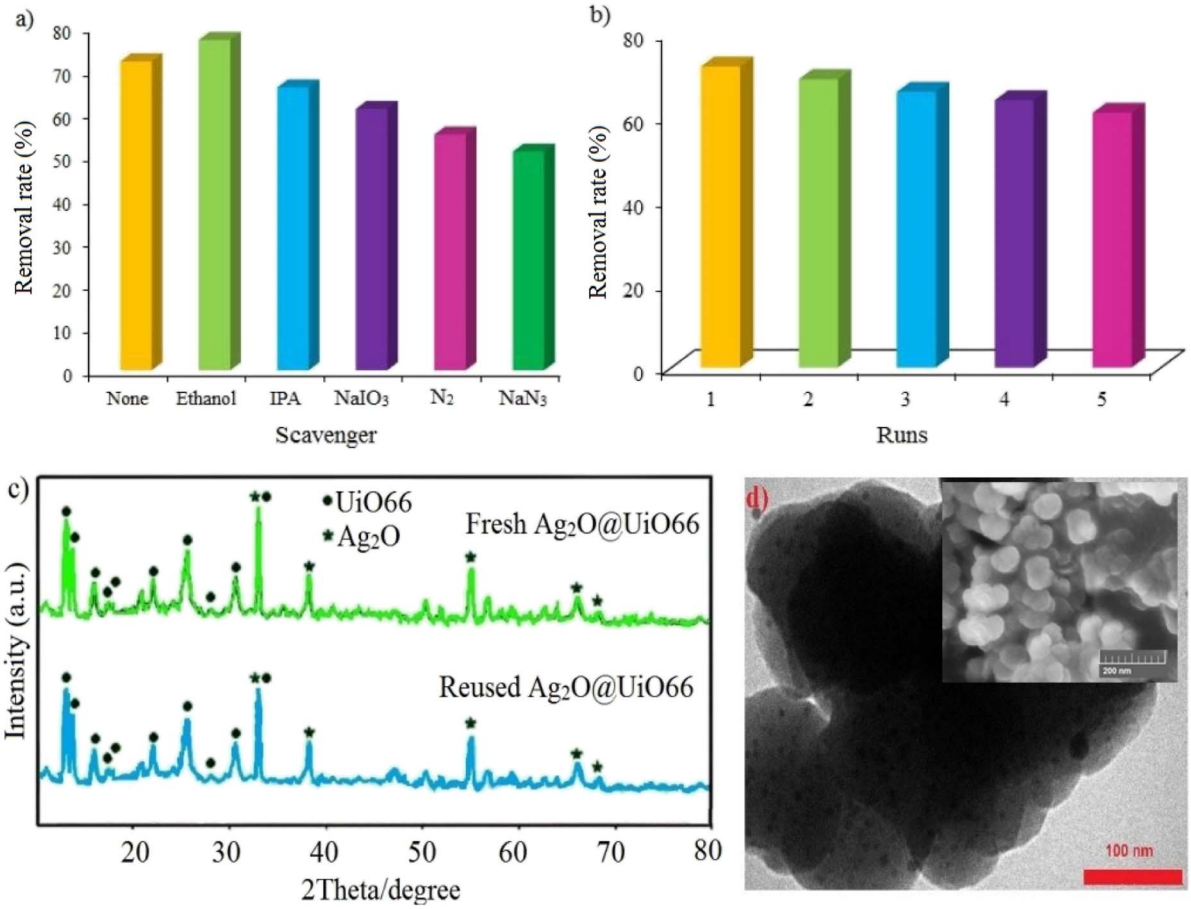

Fig. 8 (a) Effect of some scavengers on the photocatalytic process, (b) reusability and stability of the Ag_2O@UiO-66 thin film for Cr(VI), (c) XRD of the reused Ag_2O@UiO-66 thin film, and (d) TEM of the reused Ag_2O@UiO-66 thin film (inset figure shows the SEM of the Ag_2O@UiO-66 thin film after Cr(VI) reduction).

$$\frac{1}{C^2} = \frac{2}{eN_D\varepsilon_0\varepsilon S^2}\left((V - V_{fb}) - \frac{KT}{e}\right) \quad (5)$$

$$N_D = \frac{1}{\text{Slop}}\left(\frac{2}{\varepsilon\varepsilon_0 e_0}\right). \quad (6)$$

In these equations, C, V, K, T, e, ε_0, ε, and S refer to the capacitance of interfacial region, applied potential, Boltzmann constant (1.3810×10^{-23} J K^{-1}), absolute temperature, charge of electron, vacuum permittivity (8.854×10^{-14} F cm^{-1}), dielectric constant (5.96), and electrochemical surface area (1 cm^2), respectively. According to eqn (6), the photogenerated electron–hole numbers is obtained from the slope of the M–S curves (Fig. 9a). The more negative V_{fb} for Ag_2O@UiO-66 (−0.577 eV) compared to UiO-66 (−0.44 eV) can be related to the increasing oxidation power of UiO-66 through the construction of the composite with Ag_2O. The smaller slope of Nyquist plot curve obtained from the impedance analysis of Ag_2O@UiO-66 compared to UiO-66 (Fig. 9b) shows the more diminish in the recombination rate of charge carriers on the surface of Ag_2O@UiO-66 in comparision with UiO-66.

3.6 Suggesting a reasonable reaction pathway

The proposed mechanism for the photocatalytic reduction of Cr(VI) to Cr(III) is illustrated in Fig. 10. The results of the EIS determination (Fig. 9) confirmed that Ag_2O@UiO-66 displays quicker charge carrier separation and interfacial charge transfer than UiO-66. At the UiO-66 with Ag_2O junction, the electron–hole separation efficiency is improved, leading to higher Cr(VI) removal rate.[52] The junction between p-Ag_2O and n-UiO-66 is a p–n junction due to the displacement of the band levels of Ag_2O where the energy level of CB has been raised. Photogenerated electrons from the CB of Ag_2O move to the CB of the

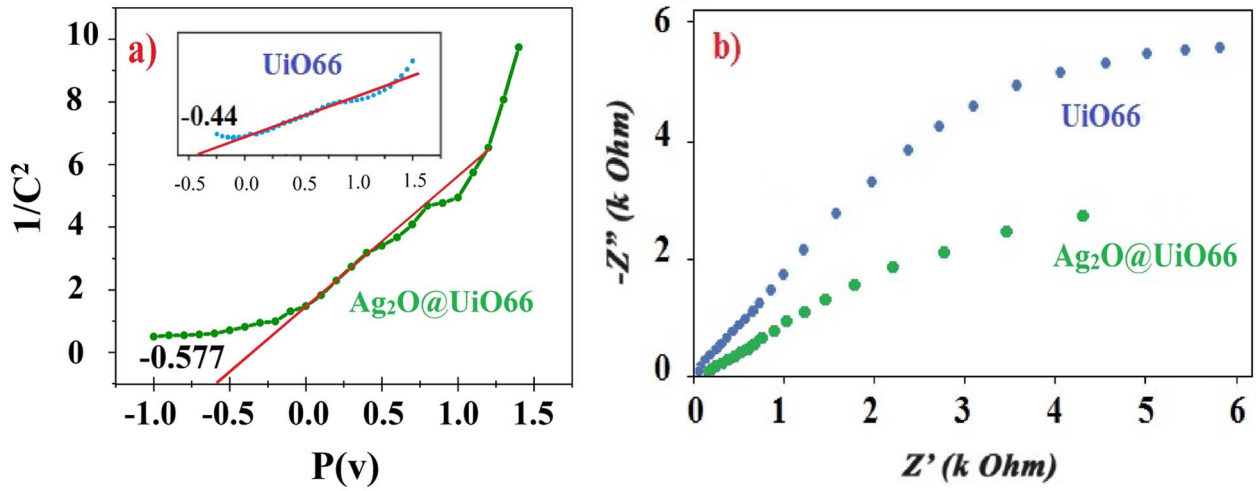

Fig. 9 (a) M–S curve and (b) EIS, Nyquist curve for Ag_2O@UiO-66 and UiO-66.

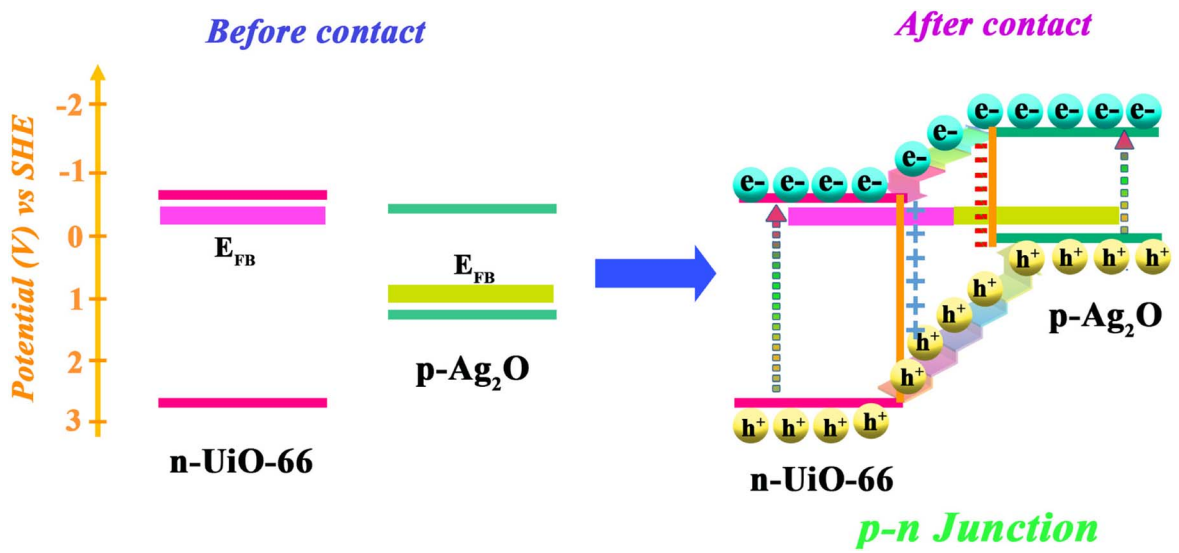

Fig. 10 Proposed mechanism of photocatalytic Cr(VI) reduction using the Ag_2O@UiO-66 thin film.

Table 2 Comparison of Ag_2O@UiO-66 with some reported catalysts in the reduction of Cr(VI) to Cr(III)

Catalyst (amount)	Concentration of Cr(VI)	Light source	Time (min)	Reduction (%)	Ref.
Ag_2O@UiO-66; thin film (0.34 g)	20 ppm	Visible-light LED	15	72	This work
$(OH)_2$–UiO-66-20% (0.4 g L^{-1})	10 mg L^{-1}	10 W LED ultraviolet	60	100	33
UiO-66-NH_2 (Zr) (17 g L^{-1})	5 ppm	300 W xenon lamp	120	98	3
UiO-66-NH_2 (Hf) (17 g L^{-1})	5 ppm	300 W xenon lamp	120	98	3
UiO-66-NH_2@BiOCl-UTNs-5 (0.5 g L^{-1})	8 mg L^{-1}	300 W Xe arc lamp	25	97	55
ZnO/$AgVO_3$ (0.2 g L^{-1})	20 mg L^{-1}	300 W Xe lamp	90	92.77	56
Ag/p-Ag_2O/*n*-$BiVO_4$ (2 mM)	15 mg L^{-1}	Visible-light	100	91.9	57
ZnO/Todorokite (200 mg L^{-1})	15 ppm	15 W mercury lamp	Unknown	97.73	7
TiO_2 (0.67 mg ML^{-1})	30 μg mL^{-1}	UV-visible (λ_{max} 540 nm)	180	~100	4
MIL-53(Fe)/SnS (1 mg mL^{-1})	20 mg L^{-1}	300 W Xe lamp	60	71.3	5
AC/*m*-TiO_2 (0.65 g L^{-1})	29.5 ppm	Xe lamp (λ_{max} 300 nm)	25	94.7	1
TPB-BT-COF (1 mg ML^{-1})	10 mg L^{-1}	Xe lamp (λ_{max} > 400 nm)	75	99	58
Bi_2S_3 thin film	22.5 ppm	Sunlight	30	98.53	59

UiO-66 component, while photogenerated holes from the VB of UiO-66 transfer to the VB of Ag_2O. This charge transfer creates an internal electric field between the two components in the Ag_2O@UiO-66 composite, which provide the crucial effect in photocatalaytic performance. Conducting the reaction in the presence of different active species scavengers determined that $^{\bullet}O_2^-$ radicals have the most effect in this reaction, which is consistent with previous reports.[53,54] On the other hand, the stainless steel mesh acts as promising substrates for photocatalytic thin films due to the webbed structure. The webbed structure of the stainless steel mesh led to light harvesting and multi-scattering of light.

3.7 Performance of Ag_2O@UiO-66 thin-film

Many reports have accounted for the reduction of Cr(VI) under photocatalytic conditions. Therefore, the present methodology was compared with some recently reported methods in terms of the most important experimental variables such as type and amount of photocatalyst, concentration of Cr(VI), light source, reaction time and reduction% (Table 2). As was mentioned before, Ag_2O@UiO-66 is the first reported thin film for the photoreduction of Cr(IV). Obviously based on the collected data in Table 2, short reaction time, use of a cheap light source, along with acceptable removal rate, are some of the advantages that make the present work comparable with others.

4 Conclusion

The EPD method was applied to the thin film preparation of all compounds over a stainless steel mesh substrate: at first, the UiO-66 metal–organic framework was prepared by a facile solvent–thermal method, and then Ag_2O nanoparticles were impregnated over the surface of UiO-66 forming the new nanocomposite Ag_2O@UiO-66. In order to achieve a suitable structure, a 30 : 70 ratio of Ag_2O : UiO-66 was determined as optimum, resulting in the best Cr(VI) removal rate due to having the lowest energy of electron transfer from the VB to CB. It showed impressive photoreduction of Cr(VI) ions in aqueous media. The UiO-66 substrate provided an interfacial potential energy field for the Ag_2O nanosphere, leading to more photogenerated charges and diminishing the recombination rate. Moreover, the p–n heterojunction between Ag_2O and UiO-66 resulted in increased charge transfer and improved the reduction rate. Finally, it can be suggested that Ag_2O@UiO-66 is a suitable candidate for removing Cr(VI) pollutants that cause a severe threat to the environment.

Author contributions

Sara Amiri: experimental, methodology, data preparation. Writing – original draft preparation. Mohammad Chahkandi: supervision, conceptualization, visualization, validation, data curation, reviewing and editing. Mahboobeh Zargazi: advisor, methodology, investigation, software, figure modification.

Conflicts of interest

The are not any conflicts to declare.

Acknowledgements

MCH gratefully thanks the Hakim Sabzevari University, Iran, for its financial support.

References

1 M. Alsaiari, *Arabian J. Chem.*, 2021, **14**, 103258.
2 H. Naeimi and M. Moradian, *Appl. Catal., A*, 2013, **467**, 400–406.
3 X. D. Du, X. H. Yi, P. Wang, W. Zheng, J. Deng and C. C. Wang, *Chem. Eng. J.*, 2019, **356**, 393–399.
4 J. B. Islam, M. Furukawa, I. Tateishi, H. Katsumata and S. Kaneco, *Chem. Eng.*, 2019, **3**, 1–10.
5 Q. Xia, B. Huang, X. Yuan, H. Wang, Z. Wu, L. Jiang, T. Xiong, J. Zhang, G. Zeng and H. Wang, *J. Colloid Interface Sci.*, 2018, **530**, 481–492.
6 R. Saha, R. Nandi and B. Saha, *J. Coord. Chem.*, 2011, **64**, 1782–1806.

7 M. Shirzad-Siboni, M. Farrokhi, R. Darvishi Cheshmeh Soltani, A. Khataee and S. Tajassosi, *Ind. Eng. Chem. Res.*, 2014, **53**, 1079–1087.
8 H. Li, T. Wu, B. Cai, W. Ma, Y. Sun, S. Gan, D. Han and L. Niu, *Appl. Catal., B*, 2015, **164**, 344–351.
9 Y. Deng, N. Kano and H. Imaizumi, *J. Chem.*, 2017, **2017**, 3426923.
10 M. Chahkandi and M. Zargazi, *J. Hazard. Mater.*, 2019, **380**, 120879.
11 M. Hua, B. Yang, C. Shan, W. Zhang, S. He, L. Lv and B. Pan, *Chemosphere*, 2017, **171**, 126–133.
12 D. Mohan, S. Rajput, V. K. Singh, P. H. Steele and C. U. Pittman, *J. Hazard. Mater.*, 2011, **188**, 319–333.
13 M. Kebir, M. Chabani, N. Nasrallah, A. Bensmaili and M. Trari, *Desalination*, 2011, **270**, 166–173.
14 R. Saha and B. Saha, *Desalin. Water Treat.*, 2014, **52**, 1928–1936.
15 R. Saha, K. Mukherjee, I. Saha, A. Ghosh, S. K. Ghosh and B. Saha, *Res. Chem. Intermed.*, 2013, **39**, 2245–2257.
16 L. Shi, T. Wang, H. Zhang, K. Chang, X. Meng, H. Liu and J. Ye, *Adv. Sci.*, 2015, **2**, 1–8.
17 Z. Zhao, H. An, J. Lin, M. Feng, V. Murugadoss, T. Ding, H. Liu, Q. Shao, X. Mai, N. Wang, H. Gu, S. Angaiah and Z. Guo, *Chem. Rec.*, 2019, **19**, 873–882.
18 H. Qi, S. Wang, H. Liu, Y. Gao, T. Wang and Y. Huang, *J. Mol. Liq.*, 2016, **215**, 402–409.
19 H. Wang, X. Yuan, Y. Wu, G. Zeng, W. Tu, C. Sheng, Y. Deng, F. Chen and J. W. Chew, *Appl. Catal., B*, 2017, **209**, 543–553.
20 W. Liu, J. Ni and X. Yin, *Water Res.*, 2014, **53**, 12–25.
21 X. Wang, Y. Liang, W. An, J. Hu, Y. Zhu and W. Cui, *Appl. Catal., B: Environ.*, 2017, **219**, 53–62.
22 S. Luo, F. Qin, Y. Ming, H. Zhao, Y. Liu and R. Chen, *J. Hazard. Mater.*, 2017, **340**, 253–262.
23 S. M. El-Sheikh, A. B. Azzam, R. A. Geioushy, F. M. El Dars and B. A. Salah, *J. Alloys Compd.*, 2021, **857**, 157513.
24 C. Xu, P. Zhao, M. Cai, Z. Dan, S. Zeng, J. Du, P. Yang and J. Xiong, *J. Photochem. Photobiol., A*, 2020, **395**, 112495.
25 T. Ge, Z. Jiang, L. Shen, J. Li, Z. Lu, Y. Zhang and F. Wang, *Sep. Purif. Technol.*, 2021, **263**, 118401.
26 F. Zhang, Y. Zhang, Y. Wang, A. Zhu and Y. Zhang, *Sep. Purif. Technol.*, 2022, **283**, 1–39.
27 Z. Huang, X. Dai, Z. Huang, T. Wang, L. Cui, J. Ye and P. Wu, *Chemosphere*, 2019, **221**, 824–833.
28 R. Karthik and S. Meenakshi, *Int. J. Biol. Macromol.*, 2014, **67**, 210–219.
29 X. Wang, Y. X. Li, X. H. Yi, C. Zhao, P. Wang, J. Deng and C. C. Wang, *Chin. J. Catal.*, 2021, **42**, 259–270.
30 W. Yang, X. Li, Y. Li, R. Zhu and H. Pang, *Adv. Mater.*, 2019, **31**, 1–35.
31 J. Bedia, V. Muelas-Ramos, M. Peñas-Garzón, A. Gómez-Avilés, J. J. Rodríguez and C. Belver, *Catalysts*, 2019, **9**, 52.
32 A. Dhakshinamoorthy, A. Santiago-Portillo, A. M. Asiri and H. Garcia, *ChemCatChem*, 2019, **11**, 899–923.
33 Y. H. Li, X. H. Yi, Y. X. Li, C. C. Wang, P. Wang, C. Zhao and W. Zheng, *Environ. Res.*, 2021, **201**, 111596.
34 S. Subudhi, L. Paramanik, S. Sultana, S. Mansingh, P. Mohapatra and K. Parida, *J. Colloid Interface Sci.*, 2020, **568**, 89–105.
35 G. Fan, J. Zhan, J. Luo, J. Lin, F. Qu, B. Du, Y. You and Z. Yan, *J. Hazard Mater.*, 2021, **404B**, 124062.
36 M. Chahkandi, M. Zargazi, A. Hajizadeh and R. Tayebee, *J. Alloys Compd.*, 2022, **902**, 163737.
37 M. Chahkandi and M. Zargazi, *J. Hazard. Mater.*, 2020, **389**, 121850, DOI: **10.1016/j.jhazmat.2019.121850**.
38 M. Chahkandi, M. Zargazi, A. Ahmadi, E. Koushki and A. Ghasedi, *RSC Adv.*, 2021, **11**, 31174–31188.
39 M. Zargazi, M. Chahkandi and M. Baghayeri, *Chemosphere*, 2022, **303**, 135079.
40 M. J. Katz, Z. J. Brown, Y. J. Colón, P. W. Siu, K. A. Scheidt, R. Q. Snurr, J. T. Hupp and O. K. Farha, *Chem. Commun.*, 2013, **49**, 9449–9451.
41 A. Kadam, R. Dhabbe, A. Gophane, T. Sathe and K. Garadkar, *J. Photochem. Photobiol., B*, 2016, **154**, 24–33.
42 S. G. Surya, S. Bhanoth, S. M. Majhi, Y. D. More, V. M. Teja and K. N. Chappanda, *CrystEngComm*, 2019, **21**, 7303–7312.
43 H. Molavi, M. Zamani, M. Aghajanzadeh, H. Kheiri Manjili, H. Danafar and A. Shojaei, *Appl. Organomet. Chem.*, 2018, **32**, 1–10.
44 Y. Feng, Q. Chen, M. Cao, N. Ling and J. Yao, *ACS Appl. Nano Mater.*, 2019, **2**, 5973–5980.
45 B. Mirhosseini-Eshkevari, M. Esnaashari and M. A. Ghasemzadeh, *ACS Omega*, 2019, **4**, 10548–10557.
46 W. M. Shume, H. C. A. Murthy and E. A. Zereffa, *J. Chem.*, 2020, DOI: **10.1155/2020/5039479**.
47 B. D. Hall, D. Zanchet and D. Ugarte, *J. Appl. Crystallogr.*, 2000, **33**, 1335–1341.
48 A. Rajabi, M. J. Ghazali, E. Mahmoudi, A. H. Baghdadi, A. W. Mohammad, N. M. Mustafah, H. Ohnmar and A. S. Naicker, *Nanomaterials*, 2019, **9**, 450.
49 S. Sadeghi, M. Jafarzadeh, A. Reza Abbasi and K. Daasbjerg, *New J. Chem.*, 2017, **41**, 12014–12027.
50 M. Humayun, A. Zada, Z. Li, M. Xie, X. Zhang, Y. Qu, F. Raziq and L. Jing, *Appl. Catal., B*, 2016, **180**, 219–226.
51 F. Narenji-Sani, R. Tayebee and M. Chahkandi, *ACS Omega*, 2020, **5**, 9999.
52 W. Zhang, L. Wang and J. Zhang, *Res. Chem. Intermed.*, 2019, **45**, 4801–4811.
53 Y. X. Li, H. Fu, P. Wang, C. Zhao, W. Liu and C. C. Wang, *Environ. Pollut.*, 2020, **256**, 113417.
54 F. Zhang, Y. Zhang, G. Zhang, Z. Yang, D. D. Dionysiou and A. Zhu, *Appl. Catal., B*, 2018, **236**, 53–63.
55 M. B. Hussain, R. Mehmood, U. Azhar, J. Wang and L. Song, *ACS Appl. Nano Mater.*, 2021, **4**, 4037–4047.
56 S. Song, K. Wu, H. Wu, J. Guo and L. Zhang, *J. Mater. Sci.*, 2020, **55**, 4987–5007.
57 W. Zhao, J. Zhang, F. Zhu, F. Mu, L. Zhang, B. Dai, J. Xu, A. Zhu, C. Sun and D. Y. C. Leung, *Chem. Eng. J.*, 2019, **361**, 1352–1362.
58 W. Chen, Z. Yang, Z. Xie, Y. Li, X. Yu, F. Lu and L. Chen, *J. Mater. Chem. A*, 2019, **7**, 998–1004.
59 M. Zargazi and M. H. Entezari, *J. Hazard. Mater.*, 2020, **384**, 121300.